Post-Print

This is the accepted version of:

Y. Wang, F. Topputo
Indirect Optimization of Fuel-Optimal Many-Revolution Low-Thrust Transfers with Eclipses
IEEE Transactions on Aerospace and Electronic Systems, Published online 08/07/2022
doi:10.1109/TAES.2022.3189330

Indirect Optimization of Fuel-Optimal Many-Revolution Low-Thrust Transfers with Eclipses

Yang Wang and Francesco Topputo
Politecnico di Milano

***Abstract*—An efficient indirect method is presented to determine fuel-optimal many-revolution low-thrust transfers in presence of Earth-shadow eclipses. Specifically, the events of shadow entrance and exit are modelled as interior-point constraints. Following the observation that an ill-conditioned state transition matrix may occur when the spacecraft flies over the edge of the shadow, a two-level continuation scheme is introduced to generate many-revolution trajectories. The established computational framework integrates analytic derivatives, switching detection and continuation with an augmented flowchart, which yields discontinuous bang-bang solutions and their gradients. Transfers from a geostationary transfer orbit to a geostationary orbit are simulated to illustrate the effectiveness and efficiency of the method developed.**

I. Introduction

SOLAR electric propulsion (SEP) enables spacecraft maneuvering with higher specific impulse, thus lowering the fuel cost compared to chemical propulsion. However, SEP-based, low-thrust Earth-orbit optimization is challenging. This is because the low thrust-to-mass radio usually requires long flight times and large number of revolutions to steer the spacecraft to the desired orbit. Additionally, the lack of power from solar panels when flying inside Earth-shadow eclipses prevents using the engine, which makes this nonlinear optimal control problem (NOCP) even more difficult to solve [1].

Numerical solution methods dedicated to low-thrust trajectory optimization are mainly categorized as direct methods, indirect methods, and dynamic programming [2]. Direct methods convert the originally infinite-dimensional NOCP into a finite-dimensional nonlinear programming (NLP) problem by direct transcription and collocation [3]. The low-thrust optimization with Earth-shadow eclipses was formulated in [4] as a large-scale multiple-phase NOCP with the phase configuration guessed a priori. In [5], shadow phases were treated as event constraints, and time-optimal transfers were determined using a state-of-the-art NLP solver. Direct collocation was developed in [6] to solve the problem that was formulated as a multi-objective, single-phase NOCP. The thrust direction was parameterized and the averaging technique was leveraged in [7–9] to reduce the computational load. Near-optimal transfers were achieved by patching trajectories generated by the Q-law and the NLP solver in [10]. Direct methods are generally robust and can easily tackle path constraints, but they often require much computational effort, especially for many-revolution trajectories [3].

Dynamic programming (DP), based on Bellman's Principle of Optimality, handles the NOCP by solving a partial differential equation, called Hamilton–Jacobi–Bellman equation [2]. The solution of DP culminates in an optimal feedback control law, instead of an open-loop solution. However, the main drawback is the curse of dimensionality, i.e., the required memory and computational time grow rapidly with dimensionality, which limits its applications to high-dimensional NOCPs [2]. A variety of DP methods have been developed to alleviate the curse of dimensionality [11]. Among them, differential dynamic programming (DDP) has been applied to various studies on trajectory optimization [12–14] and Dawn Discovery mission [15]. DDP approaches the optimal solution through a succession of quadratic subproblems around a reference trajectory [2]. The control discontinuity at shadow entrance and exit was smoothed in [12] to favor the use of the DDP technique, which culminated in approximate fuel-optimal solutions.

Alternatively, indirect methods transform the NOCP into a two-point boundary value problem by using first-order necessary conditions of optimality, the solution of which is guaranteed to be a local extremal [16]. In [17], the thrust modulus was smoothed during shadow entrance and exit to avoid the discontinuity. The Earth-shadow constraint was treated as an interior-point constraint in [18, 19] to solve time-optimal transfers, where the jump conditions of costate variables at shadow entrance and exit were derived. In [20], the averaging technique was applied to indirect optimization to rapidly search nearly time-optimal solutions. Recently, the hyperbolic tangent smoothing method was proposed in [21] to approach discontinuous control by a consecutive of continuous controls expressed by the hyperbolic tangent function, and fuel-optimal solutions with shadow constraints have been achieved in [22–24] using this method.

In practice, the performance of many optimization methods are highly dependent on the accuracy of gradient information [25]. Finite difference methods are classical gradient estimation methods that approximate the gradients by truncating

Preliminary results of this work were presented as Paper AAS 21-368 at the 31th AAS/AIAA Space Flight Mechanics Meeting, Virtual, 1–3 February 2021.

Y. Wang and F. Topputo are with the Department of Aerospace Science and Technology, Politecnico di Milano, Via La Masa 34, Italy, 20156. Email: yang.wang@polimi.it, francesco.topputo@polimi.it.

Manuscript received ..; revised ..

Taylor series of a function at a given point. These methods are easy to implement, but the accuracy relies on the selected perturbation size which is difficult to tune due to the dilemma to minimize both truncation error and subtractive cancellation error [26]. In literature, several methods have been proposed to enable highly accurate gradients. Automatic Differentiation (AD) exploits the observation that the complicated function can be expressed by the combination of elementary arithmetic operators and functions, and evaluated by repeatedly applying the chain rule [27]. Complex-step differentiation (CSD) estimates gradients by making use of complex variables [28]. The higher gradient accuracy is achieved since it elegantly eliminates the subtractive cancellation error [26, 28]. However, both AD and CSD requires extensive implementation and the execution time could be high [29]. The variational method is a promising alternative to offer accurate gradients with short computational time [25]. In this method, by propagating the variatonal equation and dynamics along with the trajectory, the gradients are estimated using state transition matrix (STM) and the chain rule [25]. Even thought the symbolic manipulations are generally required, and the integration becomes more complicated when discontinuities are involved, it is worthy to exploit it due to its high benefits on computational efficiency and gradient accuracy.

In order to expand the convergence domain, homotopy continuation methods have been widely used. The homotopy method solves the objective problem by tracking the homotopy path, which is comprised of solutions of a series of auxiliary problems [30]. In [21, 31, 32], the fuel-optimal bang-bang control was approached by a sequence of continuous controls. Moreover, pseudo-arclength method [30], double-homotopy method [33], bounding homotopy method [34] and TFC-based homotopy method [35] have been explored to tackle failures of the continuation process. The solution quality is also closely linked to the homotopy method. In [36], time-optimal transfers from a GTO to Halo orbit obtained by using bounding homotopy method perform better than the solutions in [37]. In [37, 38], the homotopy method and the variational method were combined to improve the algorithm performance.

In this work, an efficient indirect method is presented for fuel-optimal low-thrust optimization with Earth-shadow eclipses. The events of shadow entrance and exit are modelled as interior-point constraints. An analysis of STM and costate discontinuities across the shadow is carried out. Our analysis shows that ill-conditioned STM may occur when the spacecraft flies over the edge of the shadow on the optimal trajectory, which deteriorates the performance of energy-optimal to fuel-optimal continuation. Thus, a two-level continuation method is proposed to tackle this issue. The first level achieves the fuel-optimal solution without shadow constraints using energy-optimal to fuel-optimal continuation, while the second level determines the fuel-optimal solution with shadow constraints by gradually increasing the number of eclipsed arcs. The integration flowchart in [37] is augmented to involve event branches of shadow entrance and exit. The computational framework is established by combining analytic derivatives, switching detection and continuation into the augmented flowchart. The main advancement compared to previous indirect methods mentioned above is the capability to effectively compute desired discontinuous fuel-optimal bang-bang solutions for many-revolution transfers by exploiting analytic gradients and the continuation method. Transfers from a geostationary transfer orbit (GTO) to a geostationary orbit (GEO) are simulated to illustrate the effectiveness and efficiency of the method developed in applied scenarios.

The remainder of the paper is structured as follows. Section II presents dynamical equations of modified equinoctial elements, the geometrical model of Earth-shadow eclipses and fuel-optimal problem description. Section III depicts the indirect method developed. In Section IV, simulations are presented for GTO to GEO transfers. Finally, Section V concludes the work.

II. Problem Statement

A. Dynamical Equations

The modified equinoctial elements (MEE) are used to describe the orbital dynamics of the SEP-based spacecraft since they are non-singular orbital elements and are well behaved in low-thrust optimization [39]. The relationship between MEE and classical orbital elements is

$$\begin{aligned} p &= a(1-e^2) \\ e_x &= e\cos(\omega+\Omega) \\ e_y &= e\sin(\omega+\Omega) \\ h_x &= \tan(i/2)\cos\Omega \\ h_y &= \tan(i/2)\sin\Omega \\ L &= \omega+\Omega+\theta \end{aligned} \tag{1}$$

where a is the semi-major axis, e is the eccentricity, i is the orbital inclination, Ω is the right ascension of the ascending node, ω is the argument of perigee, θ is the true anomaly, p is the semilatus rectum and L is the true longitude. Equations of motion of the spacecraft under equatorial Earth-centered inertial coordinate (ECI) are

$$\dot{\boldsymbol{x}} = \boldsymbol{f}(\boldsymbol{x},\boldsymbol{\alpha},u) \Rightarrow \begin{pmatrix} \dot{\boldsymbol{x}}_{\text{mee}} \\ \dot{m} \end{pmatrix} = \begin{pmatrix} u\dfrac{T_{\max}}{m}B\boldsymbol{\alpha}+\boldsymbol{A} \\ -\dfrac{T_{\max}}{c}u \end{pmatrix} \tag{2}$$

where $\boldsymbol{x}_{\text{mee}} = [p, e_x, e_y, h_x, h_y, L]^\top$ is the MEE vector, $\boldsymbol{x} = [\boldsymbol{x}_{\text{mee}}^\top, m]^\top$ is the state vector, m is the spacecraft mass; $u \in [u_{\min}, 1]$ is the thrust throttle factor. $u_{\min} = 0$ when the SEP engine is off. $0 \le u_{\min} \le 1$ is used in the continuation scheme, see Section III-C; $\boldsymbol{\alpha}$ is the thrust direction unit vector, $T_{\max}$ is the maximum thrust magnitude, $c = I_{\text{sp}}g_0$ is the exhaust velocity where I_{sp} is the specific impulse and g_0 is the gravity acceleration at sea level. Both I_{sp} and $T_{\max}$ are assumed constant. In Eq. (2),

$$\boldsymbol{A} = [0,0,0,0,0,\kappa]^\top \tag{3}$$

$$B = \begin{bmatrix} 0 & \frac{2p}{\nu}\sqrt{\frac{p}{\mu}} & 0 \\ \sqrt{\frac{p}{\mu}}\sin L & \sqrt{\frac{p}{\mu}}[(\nu+1)\cos L + e_x]\frac{1}{\nu} & -\sqrt{\frac{p}{\mu}}[h_x \sin L - h_y \cos L]\frac{e_y}{\nu} \\ -\sqrt{\frac{p}{\mu}}\cos L & \sqrt{\frac{p}{\mu}}[(\nu+1)\sin L + e_y]\frac{1}{\nu} & \sqrt{\frac{p}{\mu}}[h_x \sin L - h_y \cos L]\frac{e_x}{\nu} \\ 0 & 0 & \sqrt{\frac{p}{\mu}}\frac{s^2}{2\nu}\cos L \\ 0 & 0 & \sqrt{\frac{p}{\mu}}\frac{s^2}{2\nu}\sin L \\ 0 & 0 & \frac{1}{\nu}\sqrt{\frac{p}{\mu}}(h_x \sin L - h_y \cos L) \end{bmatrix} \tag{4}$$

where μ is the gravitational parameter and

$$\begin{aligned} &\nu = 1 + e_x \cos L + e_y \sin L \\ &s^2 = 1 + h_x^2 + h_y^2, \quad \kappa = \sqrt{\mu p}\left(\frac{\nu}{p}\right)^2 \end{aligned} \tag{5}$$

The boundary conditions are

$$\begin{gathered} p(t_i) = p_i, \quad e_x(t_i) = e_{xi}, \quad e_y(t_i) = e_{yi}, \quad h_x(t_i) = h_{xi}, \\ h_y(t_i) = h_{yi}, \quad L(t_i) = L_i, \quad m(t_i) = m_i \\ p(t_f) = p_f, \quad e_x(t_f) = e_{xf}, \quad e_y(t_f) = e_{yf}, \quad h_x(t_f) = h_{xf}, \\ h_y(t_f) = h_{yf}, \quad L(t_f) = \text{free}, \quad m(t_f) = \text{free} \end{gathered} \tag{6}$$

where t_i and t_f are fixed initial and terminal time instants.

The MEE are related to the Cartisian coordinate $(\boldsymbol{r}, \boldsymbol{v})$ through [4]

$$\boldsymbol{r} = \begin{bmatrix} \frac{p}{s^2\nu}\left(\cos L + \alpha^2 \cos L + 2h_x h_y \sin L\right) \\ \frac{p}{s^2\nu}\left(\sin L - \alpha^2 \sin L + 2h_x h_y \cos L\right) \\ \frac{2p}{s^2\nu}\left(h_x \sin L - h_y \cos L\right) \end{bmatrix} \tag{7}$$

$$\boldsymbol{v} = \begin{bmatrix} -\frac{1}{s^2}\sqrt{\frac{\mu}{p}}\left(\sin L + \alpha^2 \sin L - 2h_x h_y \cos L \right. \\ \left. + e_y - 2e_x h_x h_y + \alpha^2 e_y\right) \\ -\frac{1}{s^2}\sqrt{\frac{\mu}{p}}\left(-\cos L + \alpha^2 \cos L + 2h_x h_y \sin L \right. \\ \left. - e_x + 2e_y h_x h_y + \alpha^2 e_x\right) \\ \frac{2}{s^2}\sqrt{\frac{\mu}{p}}\left(h_x \cos L + h_y \sin L + e_x h_x + e_y h_y\right) \end{bmatrix} \tag{8}$$

where

$$\alpha^2 = h_x^2 - h_y^2 \tag{9}$$

B. Earth-Shadow Eclipses

A shadow switching function to discriminate between eclipsed and illuminated arcs is essential. It is now derived from the shadow model. In literature, mainly two shadow models, i.e., cylindrical model [17, 18, 22] and cone model [4, 5], are widely used. The cone model in [5] is employed here since it is more accurate. When the spacecraft passes through the umbra shadow, the solar energy is completely lost, while limited solar energy is received in the penumbra shadow. To be on the safe side, we assume that the engine switches off when the spacecraft passes through either umbra or penumbra. Since umbra shadow is a portion of the penumbra shadow [4], only penumbra geometry in Fig. 1 is discussed.

Several assumptions are made to simplify the penumbra shadow model. Firstly, both the Sun and the Earth are assumed spherical bodies, thus the penumbra shadow is conical. Secondly, the Earth orbit is assumed planar and circular with

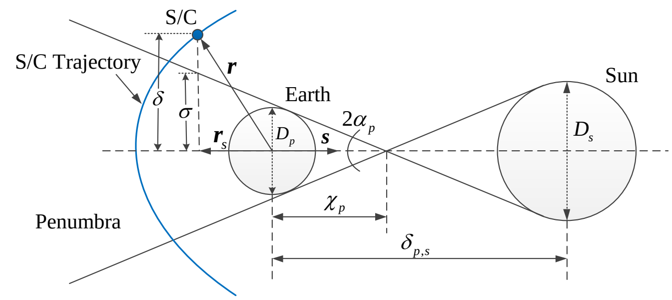

Fig. 1. Geometry of penumbra shadow (S/C: spacecraft).

respect to the Sun. In the ecliptic ECI, the Sun–Earth angle is $\theta_s = \theta_{s,i} + n(t - t_i)$, where $\theta_{s,i}$ is the Sun–Earth angle at t_i and $n = 360/365.25636306$ deg/day, and the solar unit vector is $\boldsymbol{s}_{\text{ec}} = [\cos\theta_s, \sin\theta_s, 0]^\top$. Transforming $\boldsymbol{s}_{\text{ec}}$ to $\boldsymbol{s}$ in equatorial ECI yields $\boldsymbol{s} = [\cos(\theta_s), \cos(i_e)\sin(\theta_s), \sin(i_e)\sin(\theta_s)]$, where $i_e = 23°26'21.448''$ is the ecliptic obliquity, i.e., the angle between the equatorial plane and the ecliptic plane.

Remark 1: The assumption of planar and circular Earth orbit is to simplify the computation of θ_s and its derivative $\dot{\theta}_s$. A more realistic model of the Earth orbit can be included, if accurate θ_s and $\dot{\theta}_s$ can be obtained, otherwise the performance of the indirect method may deteriorate.

In Fig. 1, D_p and D_s are diameters of the Earth and the Sun, $\delta_{p,s}$ is the distance between them, and χ_p satisfies

$$\chi_p = \frac{D_p\,\delta_{p,s}}{D_s + D_p} \tag{10}$$

The angle α_p is

$$\alpha_p = \sin^{-1}\frac{D_p}{2\chi_p} \tag{11}$$

The projection of the spacecraft position vector on the solar unit vector $\boldsymbol{s}$ is

$$\boldsymbol{r}_s = (\boldsymbol{r}\cdot\boldsymbol{s})\boldsymbol{s} \tag{12}$$

The vertical vector between the center of the penumbra cone and the spacecraft is

$$\boldsymbol{\delta} = \boldsymbol{r} - \boldsymbol{r}_s \tag{13}$$

The distance between the penumbra terminator point and the center of the penumbra cone at the projection point is

$$\sigma = (\chi_p + \|\boldsymbol{r}_s\|)\tan\alpha_p \tag{14}$$

where $\|\boldsymbol{r}_s\|$ is the Euclidean norm of $\boldsymbol{r}_s$. The difference of $\delta = \|\boldsymbol{\delta}\|$ to the distance σ is

$$S_d(t, \boldsymbol{r}) = \delta - \sigma \tag{15}$$

along with its partial derivatives as

$$\frac{\partial S_d}{\partial \boldsymbol{r}} = \frac{\boldsymbol{\delta}^\top}{\|\boldsymbol{\delta}\|}\left(\boldsymbol{I}_{3\times3} - \boldsymbol{s}\boldsymbol{s}^\top\right) - \frac{\tan\alpha_p}{\|\boldsymbol{r}_s\|}\boldsymbol{r}_s^\top\boldsymbol{s}\boldsymbol{s}^\top \tag{16}$$

$$\frac{\partial S_d}{\partial t} = -\left(\frac{\boldsymbol{\delta}^\top}{\|\boldsymbol{\delta}\|} + \frac{\boldsymbol{r}_s^\top}{\|\boldsymbol{r}_s\|}\tan\alpha_p\right)\left(\boldsymbol{r}^\top\boldsymbol{s}\boldsymbol{I}_{3\times3} + \boldsymbol{s}\boldsymbol{r}^\top\right)\frac{\partial\boldsymbol{s}}{\partial\theta_s}n \tag{17}$$

where $\partial\boldsymbol{s}/\partial\theta_s = [-\sin(\theta_s), \cos(i_e)\cos(\theta_s), \sin(i_e)\cos(\theta_s)]^\top$. The spacecraft is inside the penumbra cone if $\boldsymbol{r}\cdot\boldsymbol{s} < 0$ and

$S_d < 0$. The shadow entrance and exit occur when $S_d = 0$ and $\boldsymbol{r} \cdot \boldsymbol{s} < 0$. Thus, S_d is defined as the shadow switching function, under the condition $\boldsymbol{r} \cdot \boldsymbol{s} < 0$.

To ease the discussion, a signal variable p_{type} is defined to label the position of the spacecraft with respect to the shadow

$$p_{\text{type}} = \begin{cases} \text{In}, & \text{if} \quad S_d < 0 \quad \text{and} \quad \boldsymbol{r} \cdot \boldsymbol{s} < 0 \\ \text{Out}, & \text{otherwise} \end{cases} \tag{18}$$

To favor the explanation of the continuation scheme in Section III-C, the following definitions are given. Let $N_s(t)$ be the number of accumulated eclipses at a time t, and let $N_{\max}$ be the user-defined maximum number of eclipses. The shadow is deemed active when $N_s \leq N_{\max}$. Inactive shadows contribute to N_s, yet they do not affect the engine status. Let $\tilde{p}_{\text{type}}$ denote the spacecraft position with respect to the active shadow. Then

$$\tilde{p}_{\text{type}} = \begin{cases} \text{In}, & \text{if} \quad S_d < 0 \text{ and } \boldsymbol{r} \cdot \boldsymbol{s} < 0 \text{ and } N_s \leq N_{\max} \\ \text{Out}, & \text{if} \quad \text{otherwise} \end{cases} \tag{19}$$

Thus $\tilde{p}_{\text{type}} = p_{\text{type}}$ if sufficiently large $N_{\max}$ is adopted. If the initial point is located outside the shadow, $N_s(t_i) = 0$, otherwise, $N_s(t_i) = 0.5$. The rule $N_s \leftarrow N_s + 0.5$ is executed every time p_{type} switches its value. The updated N_s is then used to evaluate $\tilde{p}_{\text{type}}$. Thus, $N_{\max} = 0$ indicates that the shadow constraints are inactive. In Section III-C, $N_{\max}$ continuation is adopted, where $N_{\max} \leftarrow N_{\max} + 1$ is executed to gradually turn inactive shadows into active shadows.

C. Fuel-Optimal Problem

The fuel-optimal performance index is

$$J_f = \frac{T_{\max}}{c} \int_{t_i}^{t_f} u \, \mathrm{d}t \tag{20}$$

Since the optimal thrust throttle profile u^* is bang-bang [22], a continuation parameter ε is employed [37]. The performance index becomes

$$J_\varepsilon = \frac{T_{\max}}{c} \int_{t_i}^{t_f} [u - \varepsilon u(1-u)] \, \mathrm{d}t \tag{21}$$

The energy-optimal problem ($\varepsilon = 1$) is solved first, then the solution manifold is traced by gradually reducing ε, until the fuel-optimal problem ($\varepsilon = 0$) is obtained.

The Hamiltonian function reads

$$\begin{aligned} H_\varepsilon =& \frac{T_{\max}}{c} [u - \varepsilon u(1-u)] \\ &+ \lambda_L \kappa + u \frac{T_{\max}}{m} \boldsymbol{\lambda}_{\text{mee}}^\top B \boldsymbol{\alpha} - \lambda_m u \frac{T_{\max}}{c} \end{aligned} \tag{22}$$

where $\boldsymbol{\lambda} = [\boldsymbol{\lambda}_{\text{mee}}^\top, \lambda_m]^\top$ is the costate vector associated to $\boldsymbol{x}$, and $\boldsymbol{\lambda}_{\text{mee}}$, λ_m, λ_L are the costates associated to MEE, m, L, respectively. By virtue of the Pontryagin minimum principle (PMP), the optimal thrust direction $\boldsymbol{\alpha}^*$ satisfies [22]

$$\boldsymbol{\alpha}^* = -\frac{B^\top \boldsymbol{\lambda}_{\text{mee}}}{\|B^\top \boldsymbol{\lambda}_{\text{mee}}\|} \tag{23}$$

Substituting $\boldsymbol{\alpha}^*$ into Eq. (22) yields

$$H_\varepsilon = \lambda_L \kappa + u \frac{T_{\max}}{c} [S_\varepsilon - \varepsilon(1-u)] \tag{24}$$

where the throttle switching function S_ε is

$$S_\varepsilon = -\frac{c}{m} \|B^\top \boldsymbol{\lambda}_{\text{mee}}\| - \lambda_m + 1 \tag{25}$$

u^* is determined by PMP and the Earth-shadow constraint (19) as

$$u^* = \begin{cases} u_{\min}, & \text{if} \quad S_\varepsilon > (1 - 2u_{\min})\varepsilon \quad \text{or} \quad \tilde{p}_{\text{type}} = \text{In} \\ \dfrac{\varepsilon - S_\varepsilon}{2\varepsilon}, & \text{if} \quad -\varepsilon < S_\varepsilon < (1 - 2u_{\min})\varepsilon \quad \text{and} \quad \tilde{p}_{\text{type}} = \text{Out} \\ 1, & \text{if} \quad S_\varepsilon < -\varepsilon \quad \text{and} \quad \tilde{p}_{\text{type}} = \text{Out} \end{cases} \tag{26}$$

Here, $u_{\min}$ applies to both eclipsed and illuminated arcs.

Remark 2: An interior-point constraint should be addressed to ensure that Eq. (26) satisfies necessary conditions of optimality, see Section II-D.

Let $\boldsymbol{y} := [\boldsymbol{x}^\top, \boldsymbol{\lambda}^\top]^\top$ be the combined state and costate vector, the motion of the spacecraft is determined by integrating the state-costate dynamics $\dot{\boldsymbol{y}} = \boldsymbol{F}(t, \boldsymbol{y})$, i.e.,

$$\begin{cases} \dot{\boldsymbol{x}}_{\text{mee}} &= u \dfrac{T_{\max}}{m} B \boldsymbol{\alpha} + \boldsymbol{A} \\ \dot{m} &= -\dfrac{T_{\max}}{c} u \\ \dot{\boldsymbol{\lambda}}_{\text{mee}} &= -\lambda_L \left[\dfrac{\partial \kappa}{\partial \boldsymbol{x}_{\text{mee}}} \right]^\top - u \dfrac{T_{\max}}{m} \left[\dfrac{\partial B^\top \boldsymbol{\lambda}_{\text{mee}}}{\partial \boldsymbol{x}_{\text{mee}}} \right]^\top \boldsymbol{\alpha} \\ \dot{\lambda}_m &= u \dfrac{T_{\max}}{m^2} \boldsymbol{\lambda}_{\text{mee}}^\top B \boldsymbol{\alpha} \end{cases} \tag{27}$$

with $\boldsymbol{\alpha}$ and u as in Eqs. (23) and (26), respectively.

Since the terminal true longitude and mass are free, there exists

$$\lambda_L(t_f) = 0, \quad \lambda_m(t_f) = 0 \tag{28}$$

D. Interior-Point Constraint

The SEP engine switches on/off when the spacecraft exits/enters Earth-shadow eclipses. However, this operation maybe not optimal since it is not related to the minimization of H_ε. In order to satisfy necessary conditions of optimality, the events of shadow entrance and exit should be treated as interior-point constraints [18]. Let t_s be the time of either entrance or exit of the active eclipse, then $\tilde{p}_{\text{type}}$ switches between In and Out at t_s, and the following conditions should be satisfied [16]

$$H_\varepsilon(t_s^-) = H_\varepsilon(t_s^+) - \pi_\varepsilon \frac{\partial S_d}{\partial t}(t_s) \tag{29}$$

$$\boldsymbol{\lambda}_{\text{mee}}^\top(t_s^-) = \boldsymbol{\lambda}_{\text{mee}}^\top(t_s^+) + \pi_\varepsilon \frac{\partial S_d}{\partial \boldsymbol{x}_{\text{mee}}}(t_s) \tag{30}$$

where t_s^- and t_s^+ are time instants instantaneously before and after t_s, and π_ε is a scalar Lagrange multiplier. In Eq. (30), costate $\boldsymbol{\lambda}_{\text{mee}}$ is discontinuous since $\partial S_d / \partial \boldsymbol{x}_{\text{mee}}(t_s) \neq \boldsymbol{0}^\top$. It can be verified that

$$\frac{\partial \boldsymbol{r}}{\partial \boldsymbol{x}_{\text{mee}}} B = \boldsymbol{0}_{3\times3} \tag{31}$$

Since $S_d(t, \boldsymbol{r})$ is the function of t and $\boldsymbol{r}$, there exists

$$\begin{aligned} B^\top \boldsymbol{\lambda}_{\text{mee}}(t_s^+) &= B^\top \left[\boldsymbol{\lambda}_{\text{mee}}(t_s^-) - \pi_\varepsilon \left(\frac{\partial S_d}{\partial \boldsymbol{x}_{\text{mee}}} \right)^\top \right] \\ &= B^\top \boldsymbol{\lambda}_{\text{mee}}(t_s^-) - \pi_\varepsilon \left(\frac{\partial \boldsymbol{r}}{\partial \boldsymbol{x}_{\text{mee}}} B \right)^\top \left(\frac{\partial S_d}{\partial \boldsymbol{r}} \right)^\top \\ &= B^\top \boldsymbol{\lambda}_{\text{mee}}(t_s^-) \end{aligned} \tag{32}$$

Thus $\boldsymbol{\alpha}^*$ in Eq. (23) and S_ε in Eq. (25) are continuous across t_s. The time derivative of S_d is simplified as

$$\dot{S}_d = \frac{\partial S_d}{\partial \boldsymbol{x}_{\text{mee}}} \left(\boldsymbol{A} + u \frac{T_{\max}}{m} B \boldsymbol{\alpha} \right) + \frac{\partial S_d}{\partial t} = \frac{\partial S_d}{\partial L} \kappa + \frac{\partial S_d}{\partial t} \tag{33}$$

The Hamiltonian function at t_s^- and t_s^+ is

$$H_\varepsilon(t_s^-) = \lambda_L(t_s^-)\kappa + u(t_s^-) \frac{T_{\max}}{c} \left(S_\varepsilon - \varepsilon + \varepsilon u(t_s^-) \right) \tag{34}$$

$$H_\varepsilon(t_s^+) = \lambda_L(t_s^+)\kappa + u(t_s^+) \frac{T_{\max}}{c} \left(S_\varepsilon - \varepsilon + \varepsilon u(t_s^+) \right) \tag{35}$$

Combining Eq. (29), (30), (33), (34) and (35) yields the analytical expression of π_ε as

$$\pi_\varepsilon = \Delta u \frac{T_{\max}}{c} \frac{S_\varepsilon - \varepsilon + (u(t_s^+) + u(t_s^-))\varepsilon}{\dot{S}_d} \tag{36}$$

where $\Delta u = u(t_s^+) - u(t_s^-)$, $u(t_s^+) = u_{\min}$ at shadow entrance and $u(t_s^-) = u_{\min}$ at shadow exit.

Remark 3: Let $\boldsymbol{y}(t) = \boldsymbol{\varphi}_\varepsilon([\boldsymbol{x}_i, \boldsymbol{\lambda}_i], t_i, t)$ be the solution flow of Eq. (27) integrated from the initial time t_i to a generic time t, using $\boldsymbol{x}_i$, $\boldsymbol{\lambda}_i$ at t_i, u^* in Eq. (26), $\boldsymbol{\alpha}^*$ in Eq. (23) and $\boldsymbol{\lambda}_{\text{mee}}(t_s^+)$ in Eq. (30). The energy-to-fuel-optimal problem is to find $\boldsymbol{\lambda}_i^*$ such that $\boldsymbol{y}(t_f) = \boldsymbol{\varphi}_\varepsilon([\boldsymbol{x}_i, \boldsymbol{\lambda}_i^*], t_i, t_f)$ satisfies Eqs. (6) and (28).

III. Indirect Method

A. Analytic Derivatives

The variational method evaluates the gradients through the state transition matrix (STM) and the chain rule. The STM maps small variations in the initial conditions $\delta \boldsymbol{y}_i$ over $t_i \to t$, i.e., $\delta \boldsymbol{y} = \Phi(t, t_i)\delta \boldsymbol{y}_i$. The STM is subject to

$$\dot{\Phi}(t, t_i) = D_y \boldsymbol{F}\, \Phi(t, t_i) \tag{37}$$

where $D_y \boldsymbol{F}$, the Jacobian matrix of dynamical equations Eq. (27), has two different expressions based on whether u is constant or not. $\Phi(t_i, t_i) = I_{14\times14}$. Let $\boldsymbol{z} := [\boldsymbol{y}, \text{vec}(\Phi)]$ be the 210-dimensional vector consisting of $\boldsymbol{y}$ and the columns of Φ, where the operator 'vec' converts the matrix into a column vector. There exists

$$\dot{\boldsymbol{z}} = \boldsymbol{G}(\boldsymbol{z}) \Rightarrow \begin{cases} \dot{\boldsymbol{y}} & = \boldsymbol{F}(\boldsymbol{y}) \\ \text{vec}(\dot{\Phi}) & = \text{vec}(D_y \boldsymbol{F}\, \Phi) \end{cases} \tag{38}$$

Note that the integration of Φ matrix maps states and costates along a continuous trajectory. When the discontinuity is encountered at the switching time t_s, the STM compensation matrix, $\Psi(t_s)$, across the discontinuity should be determined [40]. Suppose that there are N discontinuities at $t_1,\ t_2, \cdots, t_N$, $\Phi(t_f, t_i)$ is calculated through the chain rule as

$$\begin{aligned} \Phi(t_f, t_i) =& \Phi(t_f, t_N^+)\Psi(t_N)\Phi(t_N^-, t_{N-1}^+)\Psi(t_{N-1}) \dots \\ & \dots \Phi(t_2^-, t_1^+)\Psi(t_1)\Phi(t_1^-, t_i) \end{aligned} \tag{39}$$

Suppose that the discontinuity detected at t_s is indicated by a switching function S crossing a threshold η, there are two possible cases that require to compute $\Psi(t_s)$:

- Case 1: $S = S_\varepsilon$, $\varepsilon = 0$, $\eta = 0$ in the fuel-optimal problem. In this case, $\boldsymbol{y}$ is continuous but $\dot{\boldsymbol{y}}$ is discontinuous. The thrust throttle u jumps between 0 and 1 at t_s.
- Case 2: $S = S_d$, $\eta = 0$ for the energy-to-fuel-optimal problem. In this case, both $\boldsymbol{y}$ and $\dot{\boldsymbol{y}}$ are discontinuous. The thrust throttle u jumps between $u(t_s^\pm)$ and $u_{\min}$ at t_s, if $u(t_s^\pm) \neq u_{\min}$.

For both cases, the switching function S at $t_s^- + \mathrm{d}t_s$ of the neighboring extremal trajectory must satisfy

$$S(\boldsymbol{y}(t_s^- + \mathrm{d}t_s), t_s^- + \mathrm{d}t_s) = \eta \tag{40}$$

Expanding S at t_s^- yields

$$\begin{aligned} \mathrm{d}S &= \frac{\partial S}{\partial \boldsymbol{y}} \mathrm{d}\boldsymbol{y}(t_s^-) + \frac{\partial S}{\partial t} \mathrm{d}t_s \\ &= \left(\frac{\partial S}{\partial \boldsymbol{y}} \delta \boldsymbol{y}(t_s^-) + \frac{\partial S}{\partial \boldsymbol{y}} \dot{\boldsymbol{y}}(t_s^-)\delta t_s \right) + \frac{\partial S}{\partial t} \delta t_s = 0 \end{aligned} \tag{41}$$

thus there exists

$$\delta t_s = -\frac{1}{\dot{S}} \frac{\partial S}{\partial \boldsymbol{y}} \delta \boldsymbol{y}(t_s^-) \tag{42}$$

In Case 1, since $\boldsymbol{y}$ is continuous across t_s, there satisfies

$$\boldsymbol{y}(t_s^+) = \boldsymbol{y}(t_s^-) \tag{43}$$

Taking full differentials on both sides of Eq. (43) yields

$$\delta \boldsymbol{y}(t_s^+) = \delta \boldsymbol{y}(t_s^-) + (\dot{\boldsymbol{y}}(t_s^-) - \dot{\boldsymbol{y}}(t_s^+))\delta t_s \tag{44}$$

Substituting Eq. (42) into Eq. (44) yields $\Psi(t_s)$ as

$$\Psi(t_s) = \frac{\partial \boldsymbol{y}(t_s^+)}{\partial \boldsymbol{y}(t_s^-)} = I_{14\times14} + \left(\dot{\boldsymbol{y}}(t_s^+) - \dot{\boldsymbol{y}}(t_s^-) \right) \frac{1}{\dot{S}_\varepsilon} \frac{\partial S_\varepsilon}{\partial \boldsymbol{y}} \tag{45}$$

In Case 2, $\boldsymbol{y}(t_s^+)$ is computed as

$$\boldsymbol{y}(t_s^+) = \boldsymbol{y}(t_s^-) + \Delta \boldsymbol{y} \tag{46}$$

where $\Delta \boldsymbol{y} = [\boldsymbol{0}_{7\times1}, \Delta\boldsymbol{\lambda}_{\text{mee}}, 0]$ and $\Delta\boldsymbol{\lambda}_{\text{mee}}$ is computed by Eq. (30). Taking full differential on both sides of Eq. (46) yields

$$\delta \boldsymbol{y}(t_s^+) = \delta \boldsymbol{y}(t_s^-) + \frac{\partial \Delta \boldsymbol{y}}{\partial \boldsymbol{y}} \delta \boldsymbol{y}(t_s^-) + (\dot{\boldsymbol{y}}(t_s^-) - \dot{\boldsymbol{y}}(t_s^+) + \Delta \dot{\boldsymbol{y}})\delta t_s \tag{47}$$

where

$$\Delta \dot{\boldsymbol{y}} = \frac{\partial \Delta \boldsymbol{y}}{\partial \boldsymbol{y}} \dot{\boldsymbol{y}}(t_s^-) + \frac{\partial \Delta \boldsymbol{y}}{\partial t} \tag{48}$$

Substituting Eq. (42) into Eq. (47) yields $\Psi(t_s)$ as

$$\begin{aligned} \Psi(t_s) &= \frac{\partial \boldsymbol{y}(t_s^+)}{\partial \boldsymbol{y}(t_s^-)} \\ &= I_{14\times14} + \frac{\partial \Delta \boldsymbol{y}}{\partial \boldsymbol{y}} + \left(\dot{\boldsymbol{y}}(t_s^+) - \dot{\boldsymbol{y}}(t_s^-) - \Delta \dot{\boldsymbol{y}} \right) \frac{1}{\dot{S}_d} \frac{\partial S_d}{\partial \boldsymbol{y}} \end{aligned} \tag{49}$$

Remark 4: From Eqs. (45) and (49), it is clear that the STM becomes ill-conditioned on singular arcs indicated by either $\dot{S}_\varepsilon(t_s) = 0$ or $\dot{S}_d(t_s) = 0$. The case $\dot{S}_\varepsilon(t_s) = 0$ is not considered in this work. The case $\dot{S}_d(t_s) = 0$, implying that the spacecraft flies over the edge of the shadow at t_s, may occur for optimal trajectories with many revolutions. The ill-conditioned STM deteriorates the performance of the shooting method.

B. Switching Detection Technique

A switching time detection is twofold. First, knowing $\Psi(t_s)$ at the switching time t_s is indispensable for the accuracy of gradients. Second, the integration error accumulates across the discontinuity if the switching time is not explicitly detected. Suppose that at consecutive time instants t_k and t_{k+1}, a switching function S and the constant threshold η satisfy $(S_k - \eta) \times (S_{k+1} - \eta) < 0$, where $S_k := S(t_k, \boldsymbol{y}(t_k))$ and $S_{k+1} := S(t_{k+1}, \boldsymbol{y}(t_{k+1}))$, the switching detection in [37] is then implemented to find t_s such that $S(t_s, \boldsymbol{y}(t_s)) = \eta$. The switching detection is embedded into the integration process, with the accuracy set as 10^{-12}.

However, the assumption $(S_k - \eta) \times (S_{k+1} - \eta) < 0$ may not hold. For example, suppose the shadow entrance is detected at t_k, but the spacecraft flies out of the shadow at t_{k+1}, the time detection of the shadow exit fails since $S(t_k) = 0$. In this case, the time instant $\tilde{t}_k \in (t_k, t_{k+1})$ that satisfies $(S(\tilde{t}_k, \boldsymbol{y}(\tilde{t}_k)) - \eta) \times (S_{k+1} - \eta) < 0$ and $|S(\tilde{t}_k, \boldsymbol{y}(\tilde{t}_k))| > 10^{-12}$ is searched first using the bisection method. Then the switching time $t_s \in (\tilde{t}_k, t_{k+1})$ is detected using the method in [37].

Remark 5: It is assumed that the throttle switching time and shadow switching time do not coincide. The proposed algorithm fails if this assumption is violated. If this coincidence occurs, since shadow constraints are physical constraints and the engine switches on/off is not related to the minimization of H_ε, the costate and STM should be computed using Eqs. (30) and (49), respectively. From u^* in Eq. (26), it can be verified that costates are continuous ($\pi_\varepsilon = 0$) in this case.

C. Continuation Scheme

Since the discontinuity produced by shadow constraints narrows the convergence domain, the $N_{\max}$ continuation is proposed to approach the solution by gradually turning inactive shadows into active shadows, achieved by increasing $N_{\max}$. The combination of ε continuation and $N_{\max}$ continuation is employed.

There are mainly two possible schemes. The starter of both schemes is the solution to the energy-optimal problem without shadow constraints. The first strategy consists of determining the energy-optimal solution with shadow constraints by using $N_{\max}$ continuation, and then determining the fuel-optimal solution with shadow constraints by using ε continuation. However, this strategy maybe not effective for many-revolution transfers, since the ill-conditioned STM may occur during ε continuation process. The second strategy consists of determining the fuel-optimal solution without shadow constraints by using ε continuation, and then determining the fuel-optimal solution with shadow constraints by using $N_{\max}$ continuation.

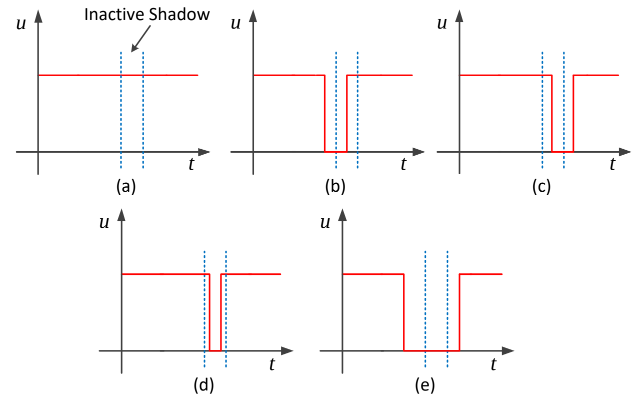

Fig. 2. Position of the inactive shadow with respect to the bang-bang thrust throttle profile.

This scheme is preferred since the ill-conditioned STM will not be encountered unless at final few steps.

Figure 2 shows five possible cases related to the position of the inactive shadow with respect to the bang-bang u profile. When the inactive shadow is switched to the active shadow, the u profile of case (e) is unchanged, while a new u profile has to be sought for cases (a)-(d). The continuation process is shown in Fig. 3, where the case (a) is employed without loss of generality. In Fig. 3, let u_ζ be the thrust throttle for $N_{\max}$–th time passage of the shadow, the fuel-optimal solution without shadow constraints ($N_{\max} = 0$ and $u_\zeta = 0$) is obtained first through ε continuation. This solution is used as the initial guess to search the fuel-optimal solution with $N_{\max} = 1$ and $u_\zeta = 0$ using the single shooting method. The algorithm may fail due to the narrow convergence domain produced by the control and costate discontinuity. Suppose that the fuel-optimal solution with $N_{\max} = 1$ and $u_\zeta = 0$ is obtained, but fails for $N_{\max} = 2$ and $u_\zeta = 0$, then the fuel-optimal problem with $N_{\max} = 2$ and $u_\zeta = 1$ is solved first. The u_ζ continuation proceeds by gradually reducing u_ζ from $u_\zeta = 1$ to $u_\zeta = 0$. Once the solution is obtained, the fuel-optimal solution with $N_{\max} = 3$ and $u_\zeta = 0$ is sought. This process continues until $N_s \leq N_{\max}$ is true, or fails due to the ill-conditioned STM.

Remark 6: Doing ε and $N_{\max}$ continuation simultaneously requires a careful design, since the total number of eclipsed arcs for the optimal trajectory is not known a priori. Additionally, the proposed continuation scheme adds one active shadow at one time. The number of active shadows added at one time is the tradeoff between convergence and computational time.

Since u^* is set to $u_{\min}$ in Eq. (26) when the spacecraft is located inside the active shadow, incorporating $N_{\max}$ continuation leads to the setting of $u_{\min}$ as

$$u_{\min} = \begin{cases} u_\zeta, & \text{if} \quad N_s > N_{\max} - 1 \quad \text{and} \quad N_s < N_{\max} \\ 0 & \text{Otherwise} \end{cases} \tag{50}$$

Thus, the value of $u_{\min}$ is set to u_ζ for $N_{\max}$-th eclipse, while $u_{\min}$ is set to 0 for the rest of the trajectory.

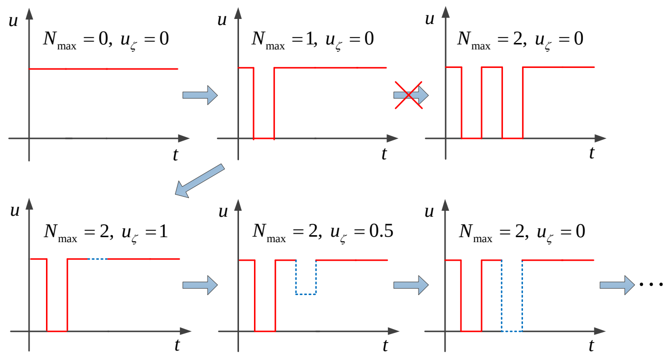

Fig. 3. $N_{\max}$ Continuation scheme from the fuel-optimal solution without shadow constraint ($N_{\max} = 0$ and $u_\varsigma = 0$) to the fuel-optimal solution with $N_{\max} = 2$ and $u_\varsigma = 0$. u_ς is the thrust throttle for $N_{\max}$–th time passage of the shadow.

D. Integration Flowchart

The integration flowchart presented in [37] is insufficient to solve low-thrust transfers involving Earth-shadow eclipses. In this section, the flowchart is augmented to involve shadow related branches.

For simplicity of discussion, let u_{type} be the engine status, the logic of which is

$$u_{\text{type}} = \begin{cases} \text{On}, & \text{if} \quad u = 1 \\ \text{Medium}, & \text{if} \quad u \in (u_{\min}, 1) \\ \text{Off}, & \text{if} \quad u = u_{\min} \end{cases} \tag{51}$$

The augmented flowchart is presented in Fig. 4. The inputs required to execute one-step integration are 1) t_k, the k–th time step; 2) h_p, the size of time step predicted by previous step of integration; 3) $\boldsymbol{z}_k$, the full 210-dimensional state; 4) u_{type}, the engine status; 5) $N_s(t)$, number of accumulated eclipses; 6) p_{type}, the position of the spacecraft with respect to the shadow defined in Eq. (18); 7) $\tilde{p}_{\text{type}}$, the position of the spacecraft with respect to the active shadow defined in Eq. (19); 8) $u_{\min}$, the minimum level of thrust throttle; 9) u_ς, the thrust throttle of the $N_{\max}$–th time of the shadow crossing.

In Fig. 4, three branches separate at the beginning of integration according to u_{type}. For each integration block, a prediction on $\boldsymbol{z}_{k+1}$, i.e., $\boldsymbol{z}_{k+1} = \boldsymbol{\psi}_{\text{RK}}(\boldsymbol{z}_k, t_k, t_k + h_p)$, is executed, using variable-step seventh/eighth Runge–Kutta integration scheme. Note that $\boldsymbol{z}_{k+1}$ is the state corresponding to $t_{k+1} = t_k + h_f$, where h_f is the corrected time step according to the integration accuracy set as 1×10^{-14}. The value of $p_{\text{type},k+1}$ corresponding to $\boldsymbol{z}_{k+1}$ is computed using Eq. (18). N_s is updated as $N_s \leftarrow N_s + 0.5$ if $p_{\text{type}} \neq p_{\text{type},k+1}$, which is then used to compute $\tilde{p}_{\text{type},k+1}$ in Eq. (19).

For u_{type} being On or Medium, execution blocks are similar. The branch of $u_{\text{type}} = \text{On}$ is depicted in the following. $u_{\text{type}} = \text{On}$ implies that $\tilde{p}_{\text{type}} = \text{Out}$ and $u_{\min} = 0$. Since the engine switches off when the active shadow is entered into, the first task after the one-step integration prediction is to check $\tilde{p}_{\text{type},k+1}$ at t_{k+1}. If $\tilde{p}_{\text{type},k+1} = \text{Out}$, the next step is to check whether p_{type} equals to $p_{\text{type},k+1}$. Even though p_{type} does not affect the status of the engine, the detection of p_{type} switching offers more information of the trajectory. If $p_{\text{type}} \neq p_{\text{type},k+1}$, Block 2 is executed to detect the shadow switching time. If $S_\varepsilon < -\varepsilon$ is satisfied, the solution is saved and p_{type} is updated to $p_{\text{type},k+1}$. Otherwise, if $S_\varepsilon \geq -\varepsilon$, it indicates that the throttle switching exists between $[t_k, t_{k+1}]$, the step h_p is reduced and N_s is rollback as $N_s \leftarrow N_s - 0.5$. When $\tilde{p}_{\text{type},k+1} = \text{Out}$ and $p_{\text{type}} = p_{\text{type},k+1}$, the same execution block on the branch $u_{\text{type}} = \text{On}$ of the flowchart in [37] is implemented. Otherwise, if $\tilde{p}_{\text{type},k+1} = \text{In}$, Block 2 is required to execute to determine the shadow switching time t_s. If $S_\varepsilon < -\varepsilon$ is satisfied, $u_{\min}$ is set by Eq. (50), Block 3 is executed, and u_{type} is set to Off.

The most complex branch is the case when $u_{\text{type}} = \text{Off}$. The first task after one-step prediction is to check $\tilde{p}_{\text{type}}$ to verify the reason that u_{type} switches Off. If $\tilde{p}_{\text{type}} = \text{In}$, implying that the spacecraft is located inside the active shadow at k–th step, the next task is to check whether the spacecraft is still inside the active shadow at t_{k+1}. If $\tilde{p}_{\text{type},k+1} = \text{In}$, the solution is saved. Otherwise, if $\tilde{p}_{\text{type},k+1} = \text{Out}$, the spacecraft flies out of the active shadow at t_{k+1}. Block 2 is executed to determine the shadow switching time t_s. The $u(t_s^+)$ instantaneous after t_s is determined by the value of S_ε with $u_{\min} = 0$. For example, if $S_\varepsilon < -\varepsilon$, u_{type} is updated to On and Block 3 is executed.

If $\tilde{p}_{\text{type}} = \text{Out}$, the spacecraft is located outside the active shadow and u_{type} switches Off due to $S_\varepsilon > \varepsilon$. If $\tilde{p}_{\text{type},k+1} = \text{In}$, the spacecraft flies inside the shadow at t_{k+1}. Then the shadow switching time is detected. Since $\Delta u = 0$, there is no need to update STM, but the shadow status is updated if $S_\varepsilon > \varepsilon$. Otherwise, if $\tilde{p}_{\text{type},k+1} = \text{Out}$ and $p_{\text{type}} = p_{\text{type},k+1}$, it indicates that the Earth's shadow is not encountered at t_{k+1}, the same execution block on the branch $u_{\text{type}} = \text{Off}$ of the flowchart in [37] is implemented.

IV. Numerical Simulations

The physical constants used are listed in Table I, where LU is the Earth radius, $\text{VU} = \sqrt{\mu/\text{LU}}$ and $\text{TU} = \text{LU}/\text{VU}$. The GTO to GEO transfer example from [22] is simulated, and the corresponding initial and terminal orbital elements are listed in Table II. Since the terminal inclination and eccentricity are both set to null, the definitions of Ω and w are invalid, thus they are set as free variables. Then the terminal conditions Eq. (6) are determined by Eq. (1). Moreover, $m_0 = 100\,\text{kg}$, $I_{\text{sp}} = 3100\,\text{s}$. All simulations are conducted under an Intel Core i7–9750H, CPU@2.6 GHz, Windows 10 system with MATLAB R2019a. The steps in ε continuation and u_ς continuation are $\Delta\varepsilon = 0.025$ and $\Delta u_\varsigma = 0.1$, respectively. Slightly larger steps $\Delta\varepsilon \leftarrow 1.01 \times \Delta\varepsilon$ and $\Delta u_\varsigma \leftarrow 1.01 \times \Delta u_\varsigma$ are used for the next step if the current step succeeds, otherwise, half of the step is used. u_ς continuation fails if $\Delta u_\varsigma < 0.005$. The maximum iteration for solving the NOCP is set as 150.

Numerical simulations for various thrust level $T_{\max} = [2, 0.5, 0.1, 0.035]$ N are executed. The corresponding energy-optimal and fuel-optimal solutions, as well as the transfer time t_f, final mass m_f, $N_{\max}$, N_s and computational time (CT) are reported in Table III. The energy-optimal solutions without shadow constraints (cases 1, 4, 7 and 10) are solved first, which is used as the starter to find fuel-optimal solutions without shadow constraints (cases 2, 5, 8 and 11) using ε continuation. Fuel-optimal solutions with shadow constraints

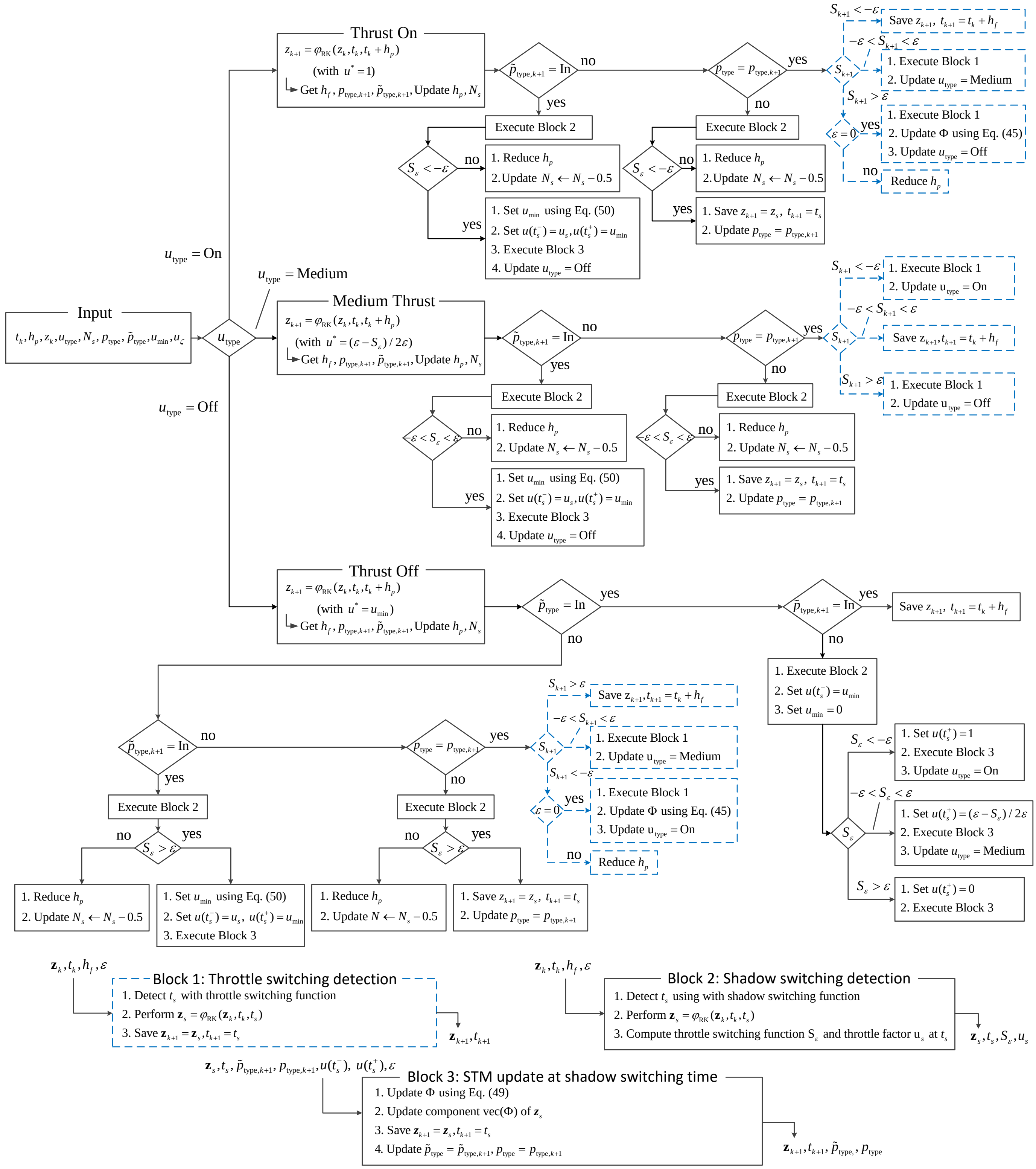

Fig. 4. Flowchart for the implementation of a generic integration step. Dashed blocks are from [37].

TABLE I
PHYSICAL CONSTANTS.

Physical constant	Value
Earth gravitational constant, μ	$398600.4418\ \mathrm{km^3/s^2}$
Gravitational field, g_0	$9.80665\ \mathrm{m/s^2}$
Length unit, LU	6378.1371 km
Time unit, TU	806.8111 s
Velocity unit, VU	7.9054 km/s
Mass unit, MU	100 kg
Earth diameter, D_p	2 LU
Sun diameter, D_s	1391020 km
Earth-Sun distance, $\delta_{p,s}$	1.4959787069×10^8 km

TABLE II
INITIAL AND TERMINAL CLASSICAL ORBIT ELEMENTS.

Type	a (km)	e	i (deg)	Ω (deg)	w (deg)	θ (deg)
GTO	24505	0.725	7	0	0	0
GEO	42165	0	0	free	free	free

for various $T_{\max}$ and $\theta_{s,i}$ (case 3, 6, 9, 12-15) are further found through $N_{\max}$ continuation. For cases with $\theta_{s,i} = 0°$ (vernal equinox departure), accurate fuel-optimal solutions are returned without encountering ill-conditioned STM for $T_{\max} = 2$ N (case 3), 0.5 N (case 6) and 0.1 N (case 9). On the other hand, approximate fuel-optimal solutions are obtained for $T_{\max} = 0.035$ N (case 12). More computational time is required when the thrust level is reduced and when ill-conditioned STM occurs. Fuel-optimal solutions for different thrust levels (cases 3, 6, 9, 12) are shown in Figs. 5. It can be seen that the shadow of fuel-optimal trajectories exists near apogee and thrust-off segments indicated by S_ε appear around perigee. From variations of u, S_ε and S_d, it can be seen that the bang-bang switching becomes more frequent as $T_{\max}$ is reduced.

More solution information of case 6 is provided. The corresponding fuel-optimal variations of a, e and i are shown in Fig. 6. Costate discontinuities produced by shadow constraints in Fig. 7 are clearly demonstrated. The computational time in this case is $\simeq 7$ mins, while the continuation fails when finite-difference method inherently embedded in MATLAB is used. The failure is caused by the inaccuracy of the finite difference method analyzed in the following. Differently from the energy-optimal to fuel-optimal continuation, the control of auxiliary solutions in the second continuation scheme is discontinuous. Based on the optimal trajectory in Fig. 5b, the gradient accuracy of the finite difference method is assessed. The Jacobian obtained by analytic gradients is used as the reference value, denoted as $J_{\mathrm{AG}}(t)$. The formula of the central finite difference method is used, as [41]

$$f'(x) = \frac{-f(x+2\eta) + 8f(x+\eta) - 8f(x-\eta) + f(x-2\eta)}{12\eta}$$

where $\eta = 1 \times 10^{-6}$ is a small perturbation step. The obtained Jacobian is denoted as $J_{\mathrm{FD}}(t)$. The gradient accuracy of the finite difference method at a given time t is calculated as the maximum value in the element of the matrix $|J_{\mathrm{FD}}(t) - J_{\mathrm{AG}}(t)|$.

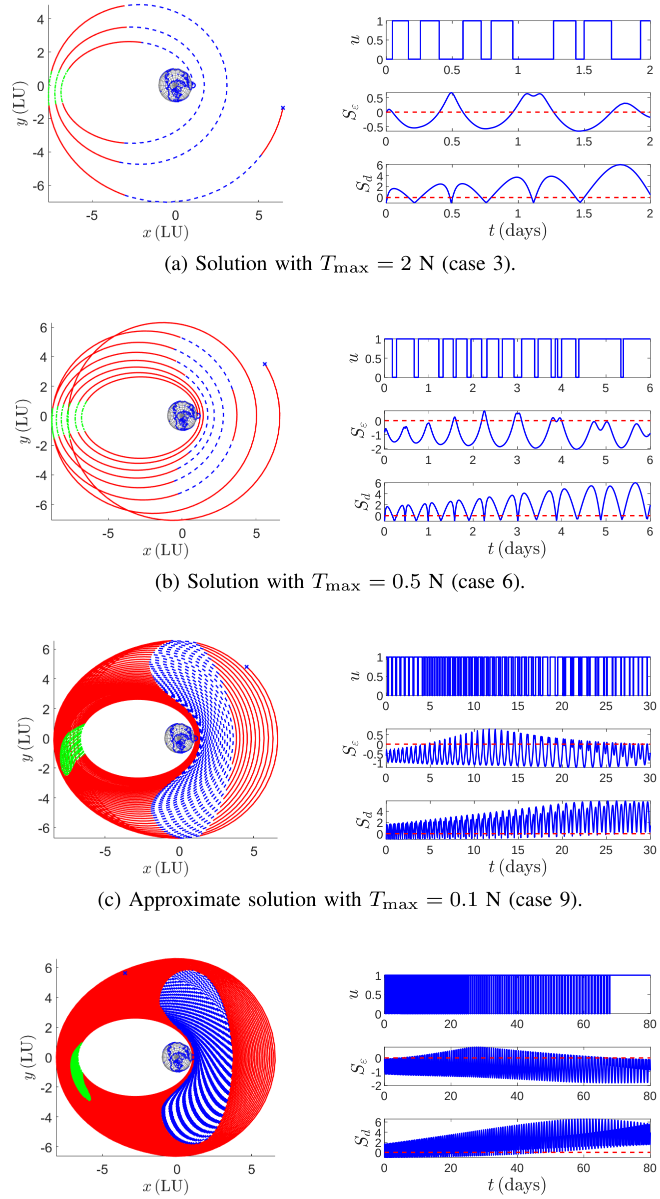

(a) Solution with $T_{\max} = 2$ N (case 3).

(b) Solution with $T_{\max} = 0.5$ N (case 6).

(c) Approximate solution with $T_{\max} = 0.1$ N (case 9).

(d) Approximate solution with $T_{\max} = 0.035$ N (case 12).

Fig. 5. Fuel-optimal solutions with different thrust levels and $\theta_{s,i} = 0°$ in Table III. Left: fuel-optimal trajectories. Blue dashed line: thrust-off segments outside shadow; red line: thrust-on segments; green dashed dot line: thrust-off segments inside shadow 'o': initial point; 'x': terminal point. Right: variations of u, S_ε, and S_d w.r.t. time. Red dash line: threshold of S_d. Line types are the same for Figs. 9 and 10.

Figure 8 shows the variation of the gradient accuracy using the finite difference method. It can be seen that the gradient accuracy deteriorates rapidly around the time of the discontinuous control and the error is accumulated as time increases. When the terminal state of an auxiliary trajectory is close to the shadow entrance and exit, the inaccurate gradient obtained by the finite difference method would deteriorate the performance of the shooting method.

Additionally, the second fuel-optimal solution for this case

TABLE III
SUMMARY OF SIMULATION RESULTS.

Case	Type	$\theta_{s,i}$	$T_{\max}$ (N)	$(\boldsymbol{\lambda}_i^*)^\top$	t_f (days)	m_f (kg)	$N_{\max}$	N_s	CT (mins)[d]
1	EO w/o[a]	/	2	$[-0.024240, -0.042279, 0.000130, 0.039448, -0.000181, -0.000083, 0.075124]$	2	93.84	/	/	/
2	FO w/o[b]	/	2	$[-0.026538, -0.062339, 0.000234, 0.033722, -0.002614, -0.000009, 0.062911]$	2	94.74	/	/	0.62
3	FO[c]	0°	2	$[-0.029159, -0.057720, -0.000427, 0.041554, -0.008385, -0.000079, 0.077206]$	2	94.22	3	3	1.54
4	EO w/o	/	0.5	$[-0.043971, -0.122824, 0.000083, 0.052453, -0.001645, 0.000040, 0.106335]$	6	93.66	/	/	/
5	FO w/o	/	0.5	$[-0.041008, -0.132771, 0.000090, 0.040169, -0.002677, 0.000098, 0.083086]$	6	94.12	/	/	1.7
6	FO	0°	0.5	$[-0.049630, -0.111368, 0.002182, 0.069476, -0.025579, -0.000004, 0.138935]$	6	93.18	8	8	7.0
7	EO w/o	/	0.1	$[-0.042528, -0.114285, 0.000011, 0.052643, -0.000245, 0.000007, 0.103373]$	30	93.73	/	/	/
8	FO w/o	/	0.1	$[-0.036987, -0.104961, 0.000024, 0.042263, -0.000462, 0.000011, 0.083938]$	30	94.15	/	/	6.0
9	FO	0°	0.1	$[-0.040920, -0.102379, 0.004436, 0.058269, -0.041627, 0.000006, 0.105747]$	30	93.63	29	29	43
10	EO w/o	/	0.035	$[-0.036844, -0.054583, 0.000016, 0.065573, -0.000096, -0.000006, 0.124880]$	80	93.67	/	/	/
11	FO w/o	/	0.035	$[-0.033988, -0.063944, 0.000014, 0.054932, -0.000116, -0.000003, 0.102696]$	80	93.96	/	/	10
12	FO	0°	0.035	$[-0.037486, -0.062639, 0.003888, 0.071624, -0.031690, -0.000004, 0.121337]$	80	93.61	49	50	95
13	FO	90°	0.035	$[-0.034889, -0.067054, -0.000268, 0.056064, -0.000141, -0.000003, 0.103954]$	80	93.94	118	118	28
14	FO	180°	0.035	$[-0.028093, -0.021725, 0.000015, 0.059236, -0.000069, -0.000007, 0.109418]$	80	93.93	87	87	26
15	FO	270°	0.035	$[-0.034330, -0.063464, -0.000270, 0.056766, 0.002185, -0.000004, 0.105290]$	80	93.92	45	45	73

[a] energy-optimal solution without shadow constraints; [b] fuel-optimal solution without shadow constraints; [c] fuel-optimal solution with shadow constraints; [d] approximate computational time starting from EO w/o.

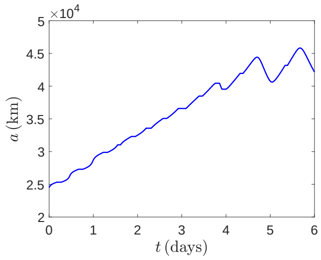

(a) Semi-major axis a.

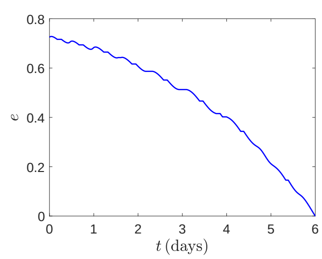

(b) Eccentricity e.

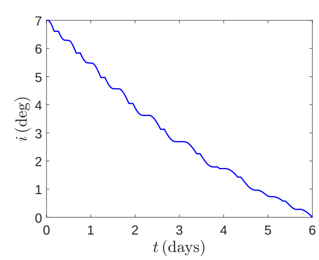

(c) Inclination i.

Fig. 6. Fuel-optimal variations of a, e and i for $T_{\max} = 0.5$ N and $\theta_{s,i} = 0°$ (case 6).

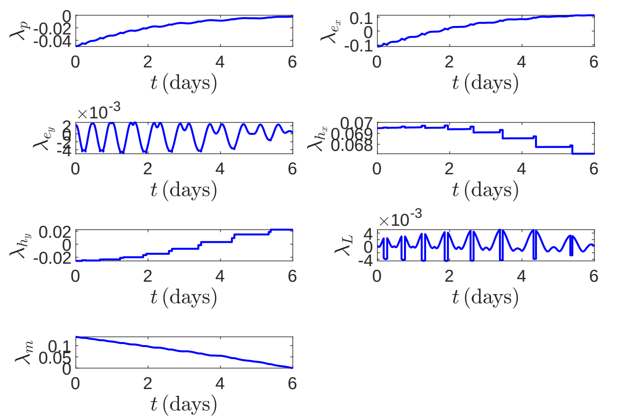

Fig. 7. Costate variations of the fuel-optimal solution for $T_{\max} = 0.5$ N and $\theta_{s,i} = 0°$ (case 6).

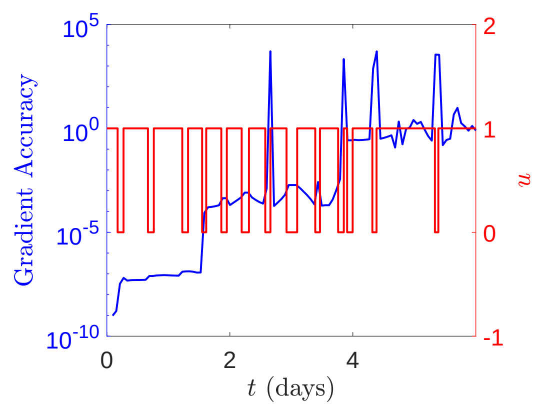

Fig. 8. Variation of the gradient accuracy w.r.t. the time using the finite difference method.

is obtained by using the first continuation scheme, as

$$\boldsymbol{\lambda}_i^* = [-0.048686, -0.049344, 0.003478, 0.093319, -0.042607, -0.000173, 0.180324]^\top$$

The corresponding fuel-optimal trajectory and variations of u, S_ε and S_d are shown in Fig. 9. The accurate bang-bang solution is returned with $N_{\max} = 8$ and $N_s = 8$. Compared to the solution in [22], both fuel-optimal trajectories pass through 8 times the shadow, and the variations of u almost coincide with each other. The final mass of fuel-optimal solution in [22] is 93.085 kg, while our solution results in 92.955 kg. The slight difference exists since the explicit time dependence of the shadow model is considered here. Compared to the hyperbolic tangent smoothing method in [22], the desired discontinuous bang-bang solution is obtained by our method. The first scheme requires only $\simeq$ 1.1 mins to obtain the solution, faster than the second scheme, but the final mass of this solution is lower than the final mass 93.18 kg obtained by the second scheme. When the finite-difference method is used, $\simeq$ 20 mins is required, taking much longer time than analytic gradients. The first continuation scheme is further used to solve

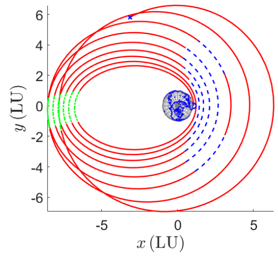

(a) Fuel-optimal trajectory.

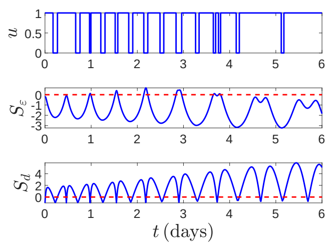

(b) Variations of u, S_ε and S_d.

Fig. 9. Second fuel-optimal solution for $T_{\max} = 0.5$ N and $\theta_{s,i} = 0°$.

cases 9 and 12. For $T_{\max} = 0.1$ N (case 9), an accurate energy-optimal solution with shadow constraints is obtained but ε continuation fails. For $T_{\max} = 0.035$ N (case 12), an approximate energy-optimal solution with shadow constraints is obtained, which fails to proceed ε continuation.

In order to further verify the effectiveness of the second scheme, fuel-optimal solutions for $T_{\max} = 0.035$ with summer solstice ($\theta_{s,i} = 90°$), autumnal equinox ($\theta_{s,i} = 180°$) and winter solstice ($\theta_{s,i} = 270°$) departures are summarized as cases 13–15 in Table III. The corresponding fuel-optimal trajectories and variations of u, S_ε and S_d are shown in Fig. 10. For all three cases, accurate solutions are obtained without encountering ill-conditioned STM, and final mass of these three cases are close to each other. For the summer solstice transfer, the spacecraft travels through the shadow region at each revolution. For autumnal equinox transfer, the initial point is located inside the shadow, and the shadow region appear in the beginning of the transfer. For the winter solstice transfer, additional shadow region appears in the last few revolutions. Simulation tests reveal that the first scheme solves cases 13 and 14 taking $\simeq$ 45 mins and $\simeq$ 70 mins, respectively, slower than the second scheme, and it fails to converge for case 15.

The comparison for both integration accuracy 1×10^{-14} and 1×10^{-16} are further executed, and the solutions coincide with each other. The computational time for accuracy 1×10^{-16} is generally longer than that for accuracy 1×10^{-14} since smaller step is used during the integration, but the exception is case 15. In this case, the computational time for accuracy 1×10^{-16} requires $\simeq$ 40 mins, shorter than the computational time for accuracy 1×10^{-14}. This is mainly because the u_ζ continuation is triggered for accuracy 1×10^{-14}, while it is not triggered for accuracy 1×10^{-16}. Therefore, higher integration accuracy generally requires longer computational time. It sometimes leads to better convergence, thus shorter computational time.

V. Conclusion

This work considers the low-thrust optimization in presence of Earth-shadow eclipses. The developed method incorporates analytic derivatives, switching detection, and continuation with an augmented integration flowchart. The advantages of the proposed indirect method include that: 1) there is no need to prescribe the thrust structure a priori; 2) it enables to find many-revolution bang-bang solutions; 3) it provides accurate gradients for robust convergence; 4) the possible ill-conditioned STM can only occur in the final few iterations. GTO to GEO mission simulations are conducted to test the algorithm performance.

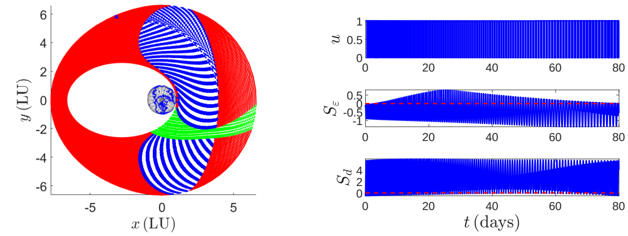

(a) Solution with $\theta_{s,i} = 90°$ (case 13).

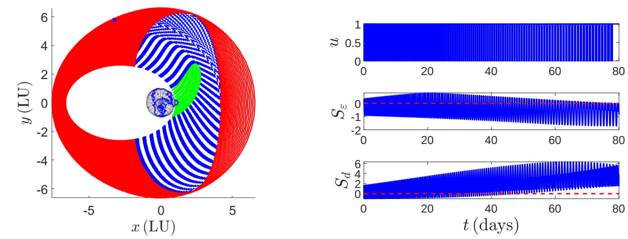

(b) Solution with $\theta_{s,i} = 180°$ (case 14).

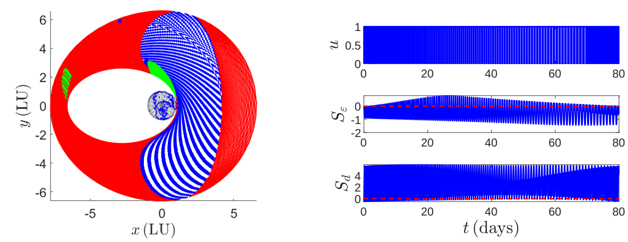

(c) Solution with $\theta_{s,i} = 270°$ (case 15).

Fig. 10. Fuel-optimal solutions for $T_{\max} = 0.035$ N and different $\theta_{s,i}$ in Table III.

Future work will consider the following issues: (1) Although the proposed flowchart suits time-optimal problems with shadow constraints as well, a more robust continuation strategy is required; (2) A higher-fidelity dynamical model, involving Earth's second zonal harmonics and Moon's perturbation, is necessary to improve the fidelity of many-revolution solutions.

Acknowledgment

Y. W. acknowledges the support of this work by the China Scholarship Council (Grant no.201706290024). The authors thank Prof. Fanghua Jiang and Prof. Lorenzo Casalino for their suggestions.

References

[1] E. Trélat, "Optimal control and applications to aerospace: some results and challenges," *Journal of Optimization Theory and Applications*, vol. 154, no. 3, pp. 713–758, 2012.

[2] D. Morante, M. Sanjurjo Rivo, and M. Soler, "A survey on low-thrust trajectory optimization approaches," *Aerospace*, vol. 8, no. 3, p. 88, 2021.

[3] F. Topputo and C. Zhang, "Survey of direct transcription for low-thrust space trajectory optimization with applications," in *Abstract and Applied Analysis*, vol. 2014. Hindawi, 2014.
[4] J. Betts, "Optimal low–thrust orbit transfers with eclipsing," *Optimal Control Applications and Methods*, vol. 36, no. 2, pp. 218–240, 2015.
[5] K. Graham and A. Rao, "Minimum-time trajectory optimization of low-thrust Earth-orbit transfers with eclipsing," *Journal of Spacecraft and Rockets*, vol. 53, no. 2, pp. 289–303, 2016.
[6] M. Leomanni, G. Bianchini, A. Garulli, R. Quartullo, and F. Scortecci, "Optimal low-thrust orbit transfers made easy: A direct approach," *Journal of Spacecraft and Rockets*, vol. 58, no. 6, pp. 1904–1914, 2021.
[7] C. Kluever and S. Oleson, "Direct approach for computing near-optimal low-thrust Earth-orbit transfers," *Journal of Spacecraft and Rockets*, vol. 35, no. 4, pp. 509–515, 1998.
[8] Y. Gao, "Near-optimal very low-thrust Earth-orbit transfers and guidance schemes," *Journal of Guidance, Control, and Dynamics*, vol. 30, no. 2, pp. 529–539, 2007.
[9] ——, "Direct optimization of low-thrust many-revolution Earth-orbit transfers," *Chinese Journal of Aeronautics*, vol. 22, no. 4, pp. 426–433, 2009.
[10] J. L. Shannon, M. T. Ozimek, J. A. Atchison, and C. M. Hartzell, "Q-law aided direct trajectory optimization of many-revolution low-thrust transfers," *Journal of Spacecraft and Rockets*, vol. 57, no. 4, pp. 672–682, 2020.
[11] N. Adurthi, P. Singla, and M. Majji, "Sparse approximation-based collocation scheme for nonlinear optimal feedback control design," *Journal of Guidance, Control, and Dynamics*, vol. 40, no. 2, pp. 248–264, 2017.
[12] J. Aziz, "Low-thrust many-revolution trajectory optimization," Ph.D. dissertation, University of Colorado at Boulder, 2018.
[13] C. Colombo, M. Vasile, and G. Radice, "Optimal low-thrust trajectories to asteroids through an algorithm based on differential dynamic programming," *Celestial mechanics and dynamical astronomy*, vol. 105, no. 1, pp. 75–112, 2009.
[14] G. Lantoine and R. Russell, "A hybrid differential dynamic programming algorithm for constrained optimal control problems. part 2: Application," *Journal of Optimization Theory and Applications*, vol. 154, no. 2, pp. 418–442, 2012.
[15] G. Whiffen, "Mystic: Implementation of the static dynamic optimal control algorithm for high-fidelity, low-thrust trajectory design," in *AIAA/AAS Astrodynamics Specialist Conference and Exhibit*, 2006, p. 6741.
[16] A. Bryson and Y.-C. Ho, *Applied Optimal Control: Optimization, Estimation and Control*. Taylor and Francis, 1975.
[17] C. Ferrier and R. Epenoy, "Optimal control for engines with electro-ionic propulsion under constraint of eclipse," *Acta Astronautica*, vol. 48, no. 4, pp. 181–192, 2001.
[18] M. Cerf, "Fast solution of minimum-time low-thrust transfer with eclipses," *Proceedings of the Institution of Mechanical Engineers, Part G: Journal of Aerospace Engineering*, vol. 233, no. 7, pp. 2699–2714, 2019.
[19] M. Pontani, "Optimal space trajectories with multiple coast arcs using modified equinoctial elements," *Journal of Optimization Theory and Applications*, vol. 191, no. 2, pp. 545–574, 2021.
[20] S. Geffroy and R. Epenoy, "Optimal low-thrust transfers with constraints—generalization of averaging techniques," *Acta Astronautica*, vol. 41, no. 3, pp. 133–149, 1997.
[21] E. Taheri and J. Junkins, "Generic smoothing for optimal bang-off-bang spacecraft maneuvers," *Journal of Guidance, Control, and Dynamics*, vol. 41, no. 11, pp. 2470–2475, 2018.
[22] R. Woollands and E. Taheri, "Optimal low-thrust gravity perturbed orbit transfers with shadow constraints," in *The 2019 AAS/AIAA Astrodynamics Specialist Conference, Portland, Maine*, 2019.
[23] E. Taheri, "Optimization of many-revolution minimum-time low-thrust trajectories using Sundman transformation," in *AIAA Scitech 2021 Forum*, 2021, paper 2021-1343.
[24] S. Singh, J. Junkins, B. Anderson, and E. Taheri, "Eclipse-conscious transfer to lunar gateway using ephemeris-driven terminal coast arcs," *Journal of Guidance, Control, and Dynamics*, vol. 44, no. 11, pp. 1972–1988, 2021.
[25] E. Pellegrini and R. Russell, "On the computation and accuracy of trajectory state transition matrices," *Journal of Guidance, Control, and Dynamics*, vol. 39, no. 11, pp. 2485–2499, 2016.
[26] W. Squire and G. Trapp, "Using complex variables to estimate derivatives of real functions," *SIAM review*, vol. 40, no. 1, pp. 110–112, 1998.
[27] P. Di Lizia, R. Armellin, A. Morselli, and F. Bernelli-Zazzera, "High order optimal feedback control of space trajectories with bounded control," *Acta Astronautica*, vol. 94, no. 1, pp. 383–394, 2014.
[28] J. Martins, P. Sturdza, and J. Alonso, "The complex-step derivative approximation," *ACM Transactions on Mathematical Software (TOMS)*, vol. 29, no. 3, pp. 245–262, 2003.
[29] D. Ellison, B. Conway, J. Englander, and M. Ozimek, "Analytic gradient computation for bounded-impulse trajectory models using two-sided shooting," *Journal of Guidance, Control, and Dynamics*, vol. 41, no. 7, pp. 1449–1462, 2018.
[30] E. Allgower and K. Georg, *Introduction to Numerical Continuation Methods*. Society for Industrial and Applied Mathematics, 2003.
[31] R. Bertrand and R. Epenoy, "New smoothing techniques for solving bang–bang optimal control problems–numerical results and statistical interpretation," *Optimal Control Applications and Methods*, vol. 23, no. 4, pp. 171–197, 2002.
[32] T. Haberkorn, P. Martinon, and J. Gergaud, "Low-thrust minimum-fuel orbital transfer: a homotopic approach,"

Journal of Guidance, Control, and Dynamics, vol. 27, no. 6, pp. 1046–1060, 2004.

[33] B. Pan, P. Lu, X. Pan, and Y. Ma, "Double-homotopy method for solving optimal control problems," *Journal of Guidance, Control, and Dynamics*, vol. 39, no. 8, pp. 1706 – 1720, 2016.

[34] X. Pan and B. Pan, "Practical homotopy methods for finding the best minimum-fuel transfer in the circular restricted three-body problem," *IEEE Access*, vol. 8, pp. 47 845–47 862, 2020.

[35] Y. Wang and F. Topputo, "A TFC-based homotopy continuation algorithm with application to dynamics and control problems," *Journal of Computational and Applied Mathematics*, vol. 401, p. 113777, 2022.

[36] X. Pan, B. Pan, and Z. Li, "Bounding homotopy method for minimum-time low-thrust transfer in the circular restricted three-body problem," *The Journal of the Astronautical Sciences*, vol. 67, no. 4, pp. 1220–1248, 2020.

[37] C. Zhang, F. Topputo, F. Bernelli-Zazzera, and Y.-S. Zhao, "Low-thrust minimum-fuel optimization in the circular restricted three-body problem," *Journal of Guidance, Control, and Dynamics*, vol. 38, no. 8, pp. 1501–1510, 2015.

[38] E. Taheri, I. Kolmanovsky, and E. Atkins, "Enhanced smoothing technique for indirect optimization of minimum-fuel low-thrust trajectories," *Journal of Guidance, Control, and Dynamics*, vol. 39, no. 11, pp. 2500–2511, 2016.

[39] J. Junkins and E. Taheri, "Exploration of alternative state vector choices for low-thrust trajectory optimization," *Journal of Guidance, Control, and Dynamics*, vol. 42, no. 1, pp. 47–64, 2019.

[40] R. Russell, "Primer vector theory applied to global low-thrust trade studies," *Journal of Guidance, Control, and Dynamics*, vol. 30, no. 2, pp. 460–472, 2007.

[41] B. Fornberg, "Generation of finite difference formulas on arbitrarily spaced grids," *Mathematics of computation*, vol. 51, no. 184, pp. 699–706, 1988.

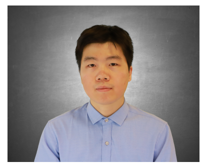

Yang Wang is a PhD candidate at the Department of Aerospace Science and Technology, Politecnico di Milano, Italy. He received his B.E. and M.S. degrees in aerospace engineering from Northwestern Polytechnical University, China, in 2014 and 2017, respectively. His research interests are in low-thrust trajectory optimization and control. E-mail: yang.wang@polimi.it.

Francesco Topputo is a Full Professor of Space Systems at Politecnico di Milano, Italy, and holds a position as Visiting Professor at TU Delft, The Netherlands. His core research activities involve spacecraft flight dynamics, interplanetary CubeSat mission and system design, autonomous guidance, navigation, and control. Dr. Topputo is an ERC laureate (CoG 2019) and has been PI in numerous research projects. He leads the Deep-space Astrodynamics Research and Technology (DART) Lab at Politecnico di Milano. E-mail: francesco.topputo@polimi.it.